Check for updates

A poorly mixed mantle transition zone and its thermal state inferred from seismic waves

Lauren Waszek [1,2 ✉], Benoit Tauzin [3,4], Nicholas C. Schmerr [5], Maxim D. Ballmer [6,7] and Juan Carlos Afonso[8]

The abrupt changes in mineralogical properties across the Earth's mantle transition zone substantially impact convection and thermochemical fluxes between the upper and lower mantle. While the 410-km discontinuity at the top of the mantle transition zone is detected with all types of seismic waves, the 660-km boundary is mostly invisible to underside P-wave reflections (P660P). The cause for this observation is debated. The dissociation of ringwoodite and garnet into lower-mantle minerals both contribute to the '660' visibility; only the garnet reaction favours material exchanges across the discontinuity. Here, we combine large datasets of SS and PP precursors, mineralogical modelling and data-mining techniques to obtain a global thermal map of the mantle transition zone, and explain the lack of P660P visibility. We find that its prevalent absence requires a chemically unequilibrated mantle, and its visibility in few locations is associated with potential temperatures greater than 1,800 K. Such temperatures occur in approximately 0.6% of Earth, indicating that the 660 is dominated by ringwoodite decomposition, which tends to impede mantle flow. We find broad regions with elevated temperatures beneath the Pacific surrounded by major volcanic hotspots, indicating plume retention and ponding of hot materials in the mantle transition zone.

Many intra-plate volcanoes are proposed to result from hot narrow upwellings that originate from the lowermost mantle[1]. Conversely, intermittent volcanic activity in the Pacific Ocean, combined with apparent motion of hotspots with respect to plate motion, indicates a shallower origin, perhaps in the mid-mantle or mantle transition zone (MTZ)[2,3]. Thus, whether large-scale upwelling encompasses the whole mantle, or occurs within semi-independent layers, remains debated[4–6]. Solid mineralogical phase changes at 410 and 660 km depths in the MTZ play a key role in regulating mantle circulation. The '410' and '660' correspond primarily to the exothermic transition from olivine (Ol) to wadsleyite (Wd), and the endothermic dissociation of ringwoodite (Rw) into bridgmanite (Br) and ferropericlase (Fp)[7], with further mineralogical reactions adding complexity. These reactions typically result in a thin MTZ in hot regions and a thick MTZ in colder environments[8]. Rw decomposition at the base of the MTZ acts to impede both cold downwellings and hot upwellings as it changes buoyancy across the phase change[6,8–15]. As reactions produce further mineral assemblages around 410 and 660 km depth, some simulations predict lateral deflection and spreading of hot upwelling material[5,16]. At high temperatures (greater than 2,100 K), another phase dissociation from majoritic garnet (Gt) to Al-bearing Mg-rich Br dominates at the base of the MTZ, and displays a Clapeyron slope with opposite sign to the Rw transition[17]. Unlike Rw decomposition, the post-Gt breakdown promotes transfer of material from the lower mantle[18,19]. Constraining the spatial extent of Gt decomposition may therefore provide clues on upwelling streams of global mantle circulation.

Currently, the maximum temperature in the MTZ, and hence the global extent of Gt decomposition dominated regions, is poorly constrained. Comprehensive information about the global temperature distribution in the MTZ can be obtained from the record of seismic waves sampling the Earth's mantle between globally distributed sources and receivers[20,21]. Translating seismic information into absolute mantle temperatures is difficult, as this requires comparing seismic observations with predictions from elastic properties at high pressure and temperature (p, T) and separating the effects of temperature from composition (see, for example, refs. [22–24]). Furthermore, different seismic datasets have their own spatial sensitivity, coverage and uncertainties that must be incorporated to avoid biases in interpretation[17,24–26].

Here, we combine global seismic datasets, mineral physics modelling and data-mining techniques to build a thermal model for the MTZ, constraining regions where Gt decomposition dominates over Rw decomposition. Progress over previous methodologies[21–23] includes an extended geographic coverage of seismic observations, and a joint analysis of data sensitive to both compressional and shear-wave velocity to alleviate trade-offs between temperature, composition and chemical equilibration models. The mineral physics analysis is further integrated into an adaptive data-driven scheme for global multi-scale model restoration, incorporating full catalogues of physics-based synthetic data. The resulting thermal model reveals that hotspots in the southern Pacific are not directly located above hot regions of the MTZ, suggesting mediated mass transfer across the mantle.

Seismic observations

Seismic studies provide first-order detailed constraints on the physical structures of the mantle. Nearly global seismic coverage of MTZ discontinuities is provided by precursors to the shear-wave phase SS and compressional equivalent PP, which travel through the mantle with one free surface reflection (Fig. 1a). Precursors (Fig. 1b) to

[1]Physical Sciences, James Cook University, Douglas, Queensland, Australia. [2]Department of Physics, New Mexico State University, Las Cruces, NM, USA. [3]Université de Lyon, UCBL, ENSL, CNRS, LGL-TPE, Villeurbanne, France. [4]Research School of Earth Sciences, Australian National University, Acton, Australian Capital Territory, Australia. [5]Department of Geology, University of Maryland College Park, College Park, MD, USA. [6]Department of Earth Sciences, University College London, London, UK. [7]Institute of Geophysics, ETH Zurich, Zurich, Switzerland. [8]Department of Earth and Planetary Sciences, Macquarie University, North Ryde, New South Wales, Australia. ✉e-mail: lauren.waszek@cantab.net
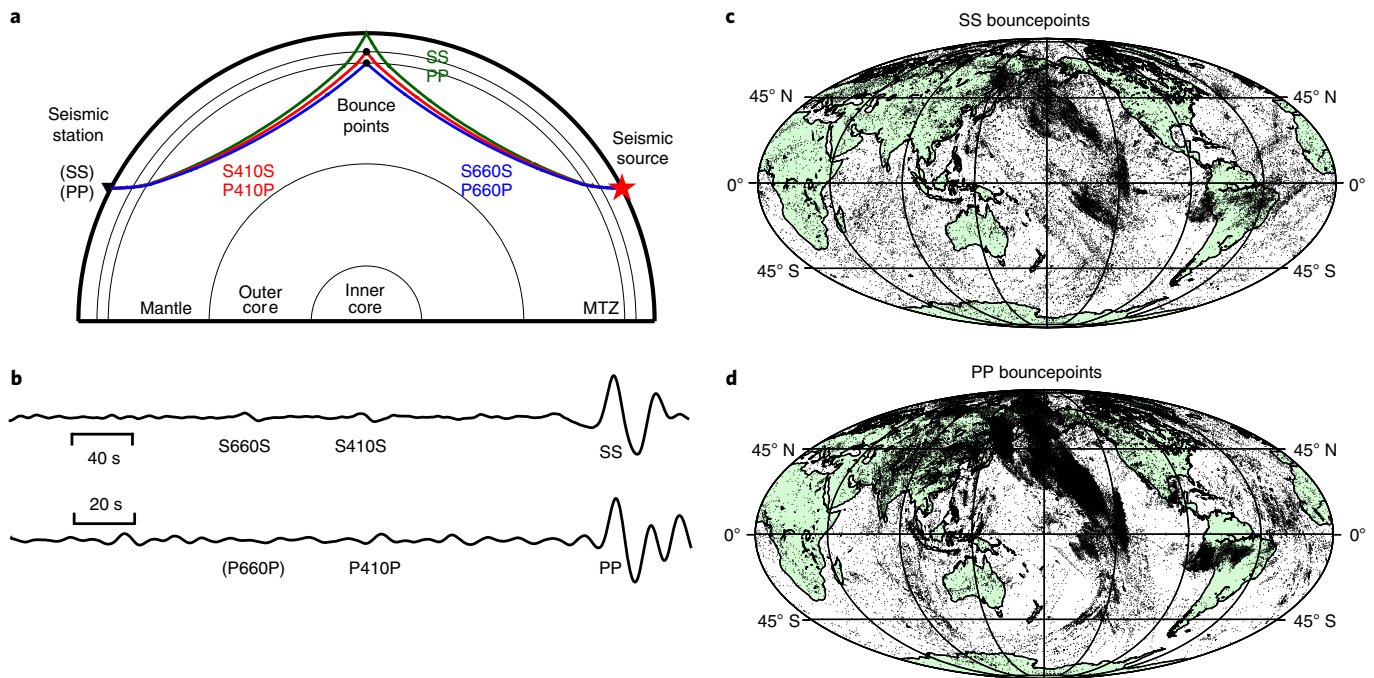
Fig. 1 | SS and PP precursory reflections underneath the 410 and 660, and global data coverage. a, Ray paths of SS and PP and their precursors S410S, S660S, P410P and P660P. **b**, Examples of high-quality SS (event in Indian Ocean, 1 January 2016, station DRLN) and PP data (Fiji, 3 January 2017, DGAR). The precursory signals from reflections at the 410 and 660 are indicated. **c**, SS bounce points of our data (Supplementary Information 1). **d**, PP bounce points.

SS and PP are generated by underside reflections from mantle discontinuities; their relative travel times are sensitive to discontinuity depths, and their amplitudes to the change in elastic properties across the discontinuity. The 410 km discontinuity is visible in both SS and PP data[17,20,21]. In contrast, the 660 is detected globally only in SS data ('S660S') but is typically absent from PP data ('P660P')[20,23].

To obtain global seismic constraints on the MTZ, we use manually picked global datasets of SS (58,217 data)[27] and PP (136,512 data) (Supplementary Information 1). The small-amplitude precursors are rarely detected in individual seismograms (Fig. 1b), thus we employ common mid-point stacking according to SS/PP bounce points (Fig. 1c,d). The individual data are corrected for 3D crustal and mantle velocity structure (SI2) using CRUST2.0[28] and S40RTS[13], with the Preliminary reference Earth model (PREM)[29] as a reference model. Global stacks reveal the 410 signal in both datasets but a missing P660P (Supplementary Fig. 1), in agreement with previous works[20,23,30]. Data are then partitioned spatially. Fixed partitioning schemes introduce geographic biases that potentially mask small-scale structure. We therefore use a stacking approach based upon global tessellations of the Earth using Voronoi cells, which adjust their size to account for sharp changes in topography, noise and data coverage (Methods and Supplementary Figs. 2–8).

This data mining approach confirms that the 410 is a global feature in both SS and PP datasets, as is the S660S. We detect substantial deviations from global average depths on regional length scales (Fig. 2, Supplementary Figs. 3 and 4, Supplementary Table 1 and Supplementary Information 3). An apparent P660P signal is detected for only around 5% of the globe (Fig. 2a). However, synthetic tests reveal that many 'detections' are likely artefacts (Methods and Supplementary Figs. 9 and 10). Almost one-third of the potential P660P patches are classified as artefacts of interfering phases, and half of the patches produce poor-quality signals (Fig. 2a and Supplementary Figs. 11 and 12). A robust P660P signal is detected in only four patches (0.6% of the globe): three in the Pacific Ocean, and one at the North Pole. Depth profiles along a cross-section through the Pacific Ocean (Fig. 2c,d) reveal narrow regions with single-peak P660P signals. Elsewhere, the 660 in PP data is broad and/or extremely low amplitude. P660P signals may exist more widely, but would be below the resolution limit of our data, or too weak to be detected within the noise. We estimate a detection threshold for P660P from seismic uncertainties on amplitude and noise levels, depending on the presence or absence of a P660P signal (Methods). A conservative estimate for the amplitude detection threshold is P660P/PP equal to 0.86%.

The S660S–S410S differential measurements and global seismic tomography models show that the visibility of P660P is associated with seismic indicators for high mantle temperatures (Supplementary Fig. 13). While the global average MTZ thickness is 244.1 ± 6.2 km, regions of robust P660P reflections display MTZ thicknesses of 238.9 ± 3.2 km (Fig. 2b). They also display lower velocities in the S40RTS tomographic model, particularly at depths of 700–1,000 km (Supplementary Fig. 13c). Statistical t tests confirmed that these differences are significant ($P < 0.001$).

Mineral physics modelling

For comparison with our data, we predict full seismic waveforms for SS and PP precursors based on mantle mineral assemblages for a range of mantle geotherms (Fig. 3a–d and Supplementary Figs. 14–19) (Methods). Phase assemblages are obtained via Gibbs free energy minimization calculations using the thermodynamic formalism from ref. [31]. We use the mineral elastic property database from ref. [32]. Properties are computed along pressure–temperature (p–T) adiabatic gradients, with defining potential temperatures (T_{pot}) associated with the extrapolation of the adiabat to zero pressure (Fig. 3a,b). Compositions are based on the chemical analysis from ref. [33].

We initially investigate the effects of temperature and composition on noise-free synthetic waveforms (Fig. 3c–f and Supplementary Figs. 18 and 19). Subsequently, we account for the exact data acquisition geometry by simulating each waveform in the
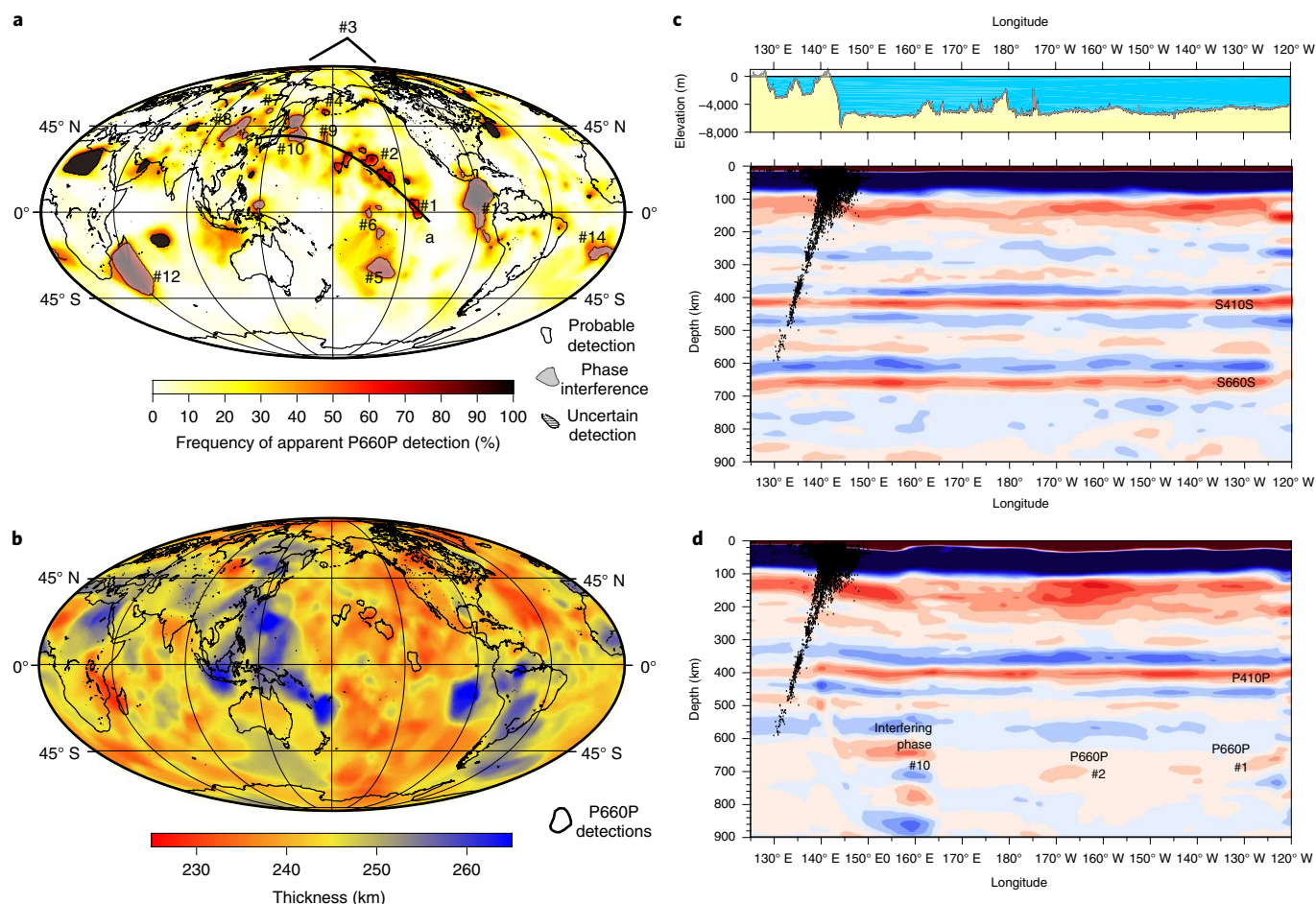
Fig. 2 | Global observations of the 410 and 660 in SS and PP data. a, Classification of apparent detections of the 660 from PP data, based on common mid-point stacking analysis. The contour of anomalies (black) is associated with a detection frequency in 50% or more of the 150 stacking parameterizations, and classified as the threshold for observation. The P660P patch labels correspond to those in Supplementary Figs. 11 and 12. **b**, Map of MTZ thickness from SS data. Robust P660P detections are superimposed. **c**, Depth profile taken along the Aa profile in **a** for SS data, calculated using 6° spherical caps with seismicity at the North Honshu subduction zone (black) and seafloor elevation as reference (inset). **d**, The corresponding depth profile for PP data reveals the effect of interfering phases near 160° E, and several actual detections of the P660P (see Supplementary Fig. 10 for modelling).

database, incorporating event depth, epicentral distance, centroid moment tensor focal mechanism solutions[34] and noise (Methods). These realistic synthetic waveforms are processed the same way as the observed data (spatial partitioning and stacking), to test predictions from compositional models (Supplementary Figs. 25 and 26). The synthetic catalogues represent a major improvement over previous one-dimensional velocity profile calculations[20], revealing important effects of data coverage and geometry, and highlighting the effects of temperature.

Compositional models are either an equilibrium assemblage (EA) of pyrolite[33], or mechanical mixtures (MM) of various proportions of basalt[35] and harzburgite[36]. Modelling mantle composition in terms of these two components considers heterogeneity that is introduced through partial melting at mid-oceanic ridges, and recycling of these heterogeneities in the deep mantle through subduction[37,38]. Mantle mixing occurs due to a combination of two mechanisms: convective shearing, which deforms distinct blobs (stirring) into thin streaks, and solid-state diffusion. These end-member processes result in two compositional models, even for the same pyrolitic chemical bulk composition of the mantle:[39] EA is chemically homogeneous and similar to the rock type peridotite in the upper mantle; MM is a solid-state mixture of basalt and harzburgite in chemical disequilibrium. Despite being based on the

same mantle bulk composition, the EA and MM models for a basalt fraction $f \approx 0.2$ exhibit differences in their mineral assemblages at a given pressure and temperature (p–T), character of related mineral reactions[38] and hence elastic properties.

This modelling approach permits us to determine (1) the thermochemical conditions of the mantle for which the SS and PP precursors are detectable, and (2) the relationship between MTZ thickness and temperatures.

A thermometer based on P660P visibility

We infer the 'visibility' of P660P by comparing amplitudes of the synthetic waveforms with the detection capability of our observational data (that is, P660P/PP greater than approximately 0.86%). This is initially performed with noise-free theoretical seismic responses, and secondly by using predictions for the same acquisition geometry as in the datasets, incorporating the effect of noise and interfering phases.

The velocity profiles for various geotherms are shown in Fig. 3a, and calculated v_p gradients in the p–T domain in Fig. 3b. Predictions from noise-free theoretical seismic responses for pyrolite EA (Fig. 3c,d) indicates that a visible P660P is associated with an increase in relative abundance of majoritic Gt at high temperature (Fig. 3b), which acts to broaden and depress the 660 discontinuity
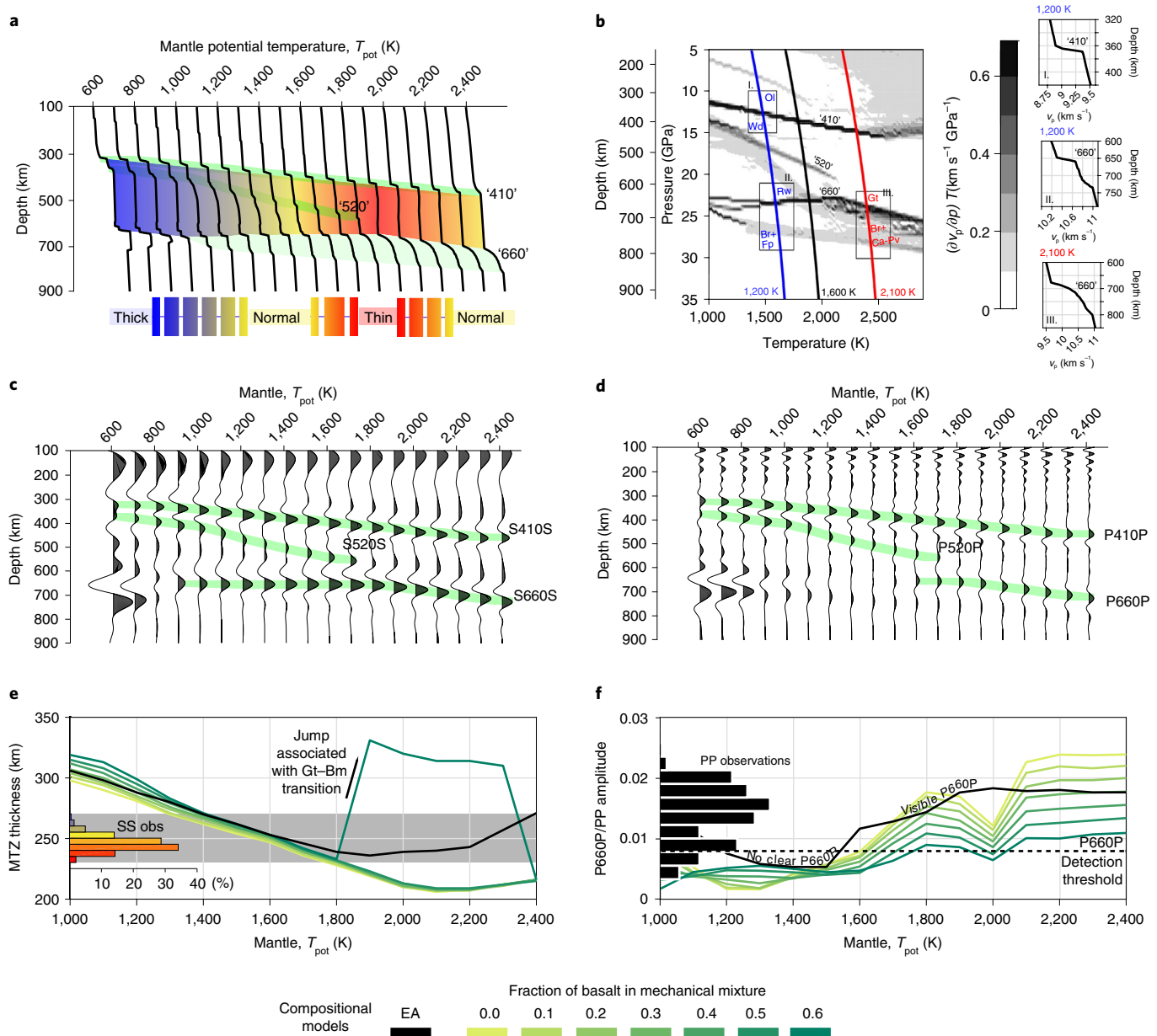
Fig. 3 | Effects of temperature on MTZ mineralogical phase transitions, and SS and PP precursors. a, The velocity structure v_s extracted for an EA of pyrolite, along a set of adiabatic temperature gradients for different potential temperatures shows that the MTZ thickness varies non-linearly with temperature. Green lines and shading indicate first-order or sharp gradients. Note that v_p and v_s have similarly shaped profiles. **b,** Diagram of P-wave velocity gradients showing the effects of temperature on the 410 and 660. The grey background scales with the amplitude of the velocity gradient, with the darkest regions associated with the sharpest and strongest gradients (insets). The shape of the gradients is a controlling parameter for reflected-wave amplitudes. Ca-Pv, calcium perovskite. **c,** Set of synthetic SS seismograms calculated for a range of temperatures in a pyrolite EA mantle. **d,** Similar set of synthetic PP seismograms. The peaks corresponding to the 410, 520 and 660 are labelled. Note that these waveforms are ideal and contain no noise. **e,f,** Predictions of the MTZ thickness from SS data (**e**) and P660P amplitude (**f**) based on EA (black) and MM with variable f (light to dark green), measured from synthetic data such as those in **c** and **d**. These predictions are compared with observations (histograms along vertical axis). Note the sharp increase in MTZ thickness from SS data at 1,800 K for a MM with $f = 0.6$, as a consequence of the emergence of the Gt–Bm reaction with larger signal amplitude (Supplementary Fig. 18). Curves in panels **e, f** are sampled with a step of 100 K and obtained by linear interpolation. This adds a ±50 K uncertainty on the P660P visibility T_{pot} threshold. Bm, bridgmanite.

to 720 km depth. This regime corresponds to potential temperatures above $T_{pot} = 1,600$ K (see, for example, inset III in Fig. 3b). We find a similar temperature-dependent P660P visibility for MM models (Fig. 3f). A notable difference is the higher visibility threshold of $T_{pot} = 1,700–1,800$ K for MM (Fig. 3f), slightly increasing with basalt fraction f. In this noise-free analysis, it is not possible to define an

exact temperature threshold for P660P visibility, as this depends on composition and data noise, both of which are spatially variable.

A prior study[23] also identified a thermal dependence of P660P visibility, but found an opposite relationship, with weak reflection amplitudes for high-T (1,900 K) geotherms. We attribute this discrepancy to their use of Zoeppritz equations to describe the
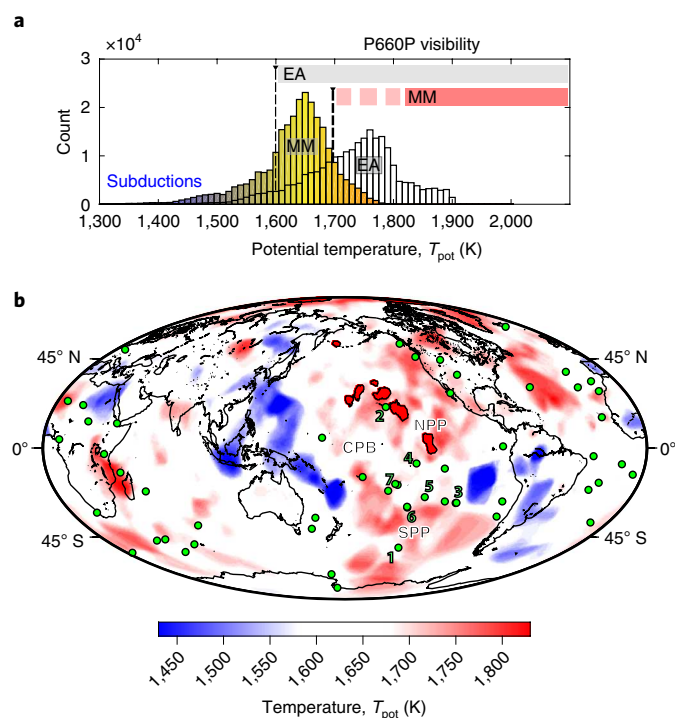
Fig. 4 | Thermal model of the MTZ and implications for global mantle circulation. a, Histograms of global mantle temperatures in the MTZ based on seismic and mineral-physics constraints. The positioning of the global average temperature and the absolute temperature threshold for the visibility of the post-Gt transition in PP data (grey and pink bars) depend on the model of mantle composition (EA or MM). We use $f = 0.2$ for MM, and colour shading indicates temperature. The P660P visibility threshold depends on the data noise level and composition (dashed pink), but cannot extend far below around 1,700 K, otherwise we would over-predict the P660P visibility. **b**, Composite model of the temperature in the MTZ based on S660S (colours) and P660P (black contours) observations with superimposed hotspot locations. The hotspot distribution (green dots) is from ref.[45] as follows: 1, Louisville; 2, Hawaii; 3, Easter; 4, Marquesas; 5, Pitcairn; 6, Austral–Cook; 7, Tahiti–Society.

partitioning of seismic wave energy at first-order interfaces, rather than considering full waveforms as we do here (Methods and Supplementary Fig. 16).

The MTZ thickness estimated from SS data (for example, Fig. 3c,e) decreases monotonically as T_{pot} increases for T_{pot} smaller than 1,800–2,100 K (depending on composition), but then increases again at very high temperatures (Fig. 3e), in contrast to a pure Ol model[22]. The main difference between EA and MM models occurs at T_{pot} greater than 1,800 K, with thinner MTZ predicted for MM (Fig. 3e).

We use our mineral-physics models to convert the observed MTZ thicknesses into a global field of vertically averaged MTZ temperature. Vertical thermal gradients would have a small influence on these measurements as the thickness is primarily controlled by the 410 topography, with influences of 0.1 km K^{-1} and 0.007 km K^{-1} for the 410 and 660, respectively (Fig. 3c and Methods). Thus, temperature estimates based on MTZ thickness are blind to thermal gradients. We find that the global average T_{pot} based on pyrolite EA is approximately 1,730 ± 50 K (Fig. 4a), in agreement with estimates from a smaller SS dataset[21]. Peak-to-peak variations are ±300 K. However, the EA model for these temperatures predicts P660P reflections over around 45% of the globe (Supplementary Fig. 25). Noting that this does not account for detection bias and

interfering phases, the prediction is clearly at odds with the observed proportion of approximately 5.0% (Fig. 2a). Furthermore, the EA model cannot account for the thinnest MTZ from SS measurements (Fig. 3e).

Performing calculations for MM with bulk pyrolitic composition (20% basalt, 80% harzburgite) resolves this discrepancy. It reduces the average T_{pot} by around 100 K to 1,630 ± 50 K (Fig. 4a), in good agreement with petrological constraints from mid-ocean ridge volcanism[40], and shifts the visibility of the P660P to higher T_{pot} (1,700–1,800 K). Thus, the thermal field for MM predicts P660P reflections over a smaller portion of the Earth (14.0%), better matching the data (Supplementary Fig. 26). This computation for basalt fractions of 0.2 represents a lower temperature bound for P660P visibility, since it favours visibility at lower T_{pot} than for higher basalt fraction. Fewer P660P observations would be predicted for higher basalt enrichments, in agreement with our global average basalt fraction estimate of approximately 0.35 (Effect of composition section and Supplementary Figs. 22–24).

A previous study[22] determined a preference for MM over EA thermal fields from SS data. However, the discrimination between models relied on petrological thermo-barometry. Here, we show that complementary PP data provide a robust constraint. Our inferred temperatures generally agree with petrologic estimates for overlying hotspot temperatures, even though the former are systematically lower than the latter (Supplementary Fig. 27), probably explained by lower seismic resolutions than typical plume radii.

Conversely, an investigation of thermochemistry using receiver functions[24] found that the mantle is better described by a patchwork of EA and MM composition, at odds with our preferred global MM model. This discrepancy is reconciled by considering the data resolution of both studies. Ps conversions sample continental areas beneath seismic stations with a maximum of approximately 500 km diameter in the MTZ, whereas the minimum lateral resolution of SS and PP precursors is approximately 600 km. Conversion data are therefore sensitive to small regions in the mantle that have potentially been fully homogenized, while reflection data sample globally a mantle that corresponds to a mechanical mixture on the relevant, longer wavelengths.

Along these lines, our modelling indicates that P660P visibility, in combination with MTZ thickness from SS precursors, can be used as a mantle thermometer. We propose that the marker for a very hot regime is thin-to-normal MTZ from SS data combined with a visible P660P, and that normal temperature conditions (T_{pot} of around 1,600 K (ref.[40])) favour a widespread 'absence' of P660P reflections.

Effect of composition
Our mineral-physics modelling further suggests that the global absence of P660P observations (Figs. 2a and 3f) is primarily explained by thermal rather than compositional effects. MM calculations predict that P660P amplitudes decrease with increasing basalt fractions (Fig. 3f and Supplementary Figs. 18–20). At high basalt fractions, it is essential to distinguish between signals of the Rw dissociation and of the deeper Gt breakdown (Fig. 3a–d and Supplementary Figs. 17–19). These signals are separable for basalt fractions smaller than a threshold of 0.7–0.8, at which point the shallower Rw signal becomes undetectable. In theory, the presence of P660P might therefore also constrain the amount of basalt enhancement near the 660 km discontinuity. This aspect is particularly appealing as the detection of basalt enrichment in the MTZ, that is, an MM with f greater than 0.2 (ref.[39]), is consistent with previous evidence for accumulations of recycled oceanic crust at the base of the MTZ from observational and modelling studies[15,26,41].

Very high basalt fractions ($f > 0.6$), however, are incompatible with our observed seismic amplitudes measurements (Supplementary Figs. 20–21). We incorporate SS and PP precursor

amplitude information with MTZ thickness in a Bayesian inversion to obtain radially averaged potential temperature and permissible basalt fractions in the MTZ (Methods and Supplementary Figs. 22–24). Globally, the best-fitting solution occurs at $T_{pot} \approx$ 1,625 K and $f \approx 0.35$, with acceptable models ranging from 1,450 to 1,650 K and from 0.18 to 0.45 (one standard deviation). For these compositions, the P660P visibility is fully controlled by the Gt dissociation (Fig. 3b) at high temperatures (Fig. 3f). In a similar inversion, locations with visible P660P (Supplementary Fig. 24) favour higher temperatures (1,750–1,800 K) and further enhanced basalt fractions (0.4–0.45).

Overall, our data are therefore consistent with a moderately basalt-enriched MTZ, quantitatively agreeing with geodynamic models[42]. We cannot rule out more extreme small-scale compositional variations with local reductions or enrichments in basalt fraction, or regions dominated by EA, especially below our resolution limit (approximately 600 km, Supplementary Fig. 28). Similarly, compositional gradients across the MTZ may occur, but such variations have limited effect on our temperature estimates and are virtually undetectable by precursors due to their limited effects on discontinuity depths (0.5 km absolute depth perturbation for a 10% increase in basalt fraction; Supplementary Fig. 24). The same holds true for compositional changes across the discontinuities. We estimate only a 6 K temperature difference for a 12% increase in f. Currently, the lack of thermodynamic data precludes considerations on the effects of minor components, such as volatiles or ferric iron[43,44].

Implications for mantle convection

The observations of P660P are thus attributed to the broad Gt decomposition dominating in the very hottest regions of the MTZ with T_{pot} greater than 1,800 K (Figs. 2 and 3). The dynamical effect of the Gt decomposition with a positive Clapeyron slope promotes upward transfer of hot material across the 660 (refs. [6,18]). Our findings for both P660P visibility and MTZ thickness suggest that such high T and thus efficient transport are reached in only a very few and small locations (Figs. 2a and 4a), detectable only in regions with the highest data coverage (Supplementary Fig. 28), which the lower-resolution S660S data cannot capture.

The P660P detections are primarily located beneath the Pacific Ocean, a region with a large concentration of hotspots (see, for example, ref. [45]), but there is no direct correlation with individual hotspots (Fig. 4b). Our thermal field (Fig. 4b) reveals two broad provinces of elevated temperatures, the North Pacific Province and South Pacific Province, separated by a central belt of 'normal' temperature: the Central Pacific Belt. The Central Pacific Belt includes the Pacific Superswell, a region of anomalously shallow seafloor associated with a geoid low and isotopic anomalies often ascribed to a low-density upwelling in the upper mantle[46]. Interestingly, the edges of the North Pacific Province and South Pacific Province are correlated with the surface expression of 13 of the 24 Pacific hotspots (Supplementary Information 6, Fig. 4b, and Supplementary Figs. 29 and 30). Many of these hotspots display intermittent activity (less than 30 Myrs), violating the classical Wilson–Morgan plume theory[3,47]. Their locations at the edges of hot provinces are inconsistent with simple vertical material transfer through the MTZ. Instead, it implies mediated mass transfer across the MTZ with (partial) failure and ponding of hot plume material for substantial timescales[4,5], secondary thermal upwellings from the edges of ponding regions where thermal convective instability is advanced[6,46,48] and only the very hottest material (greater than 1,800 K) rising straight through[5]. Such a scenario implies an indirect link between plume generation zones in the lowermost mantle[1] and hotspot locations[14].

Since Gt decomposition is only prevalent at very high temperatures, the large hot regions with T_{pot} between 1,700 and 1,800 K are dominated by Rw dissociation, which impedes vertical flow[6,8,10].

This outcome agrees with previous seismic studies that demonstrated a mainly thermal control of the 660 (refs. [21,22]). The Rw dissociation reaction is a good candidate to explain ponding of material near the 660 at the bottom of the MTZ, and other factors such as basalt content, subadiabaticity and temperature-induced viscosity contrasts probably also play a key role in plume dynamics[4–6,15,37].

Thus, our results are consistent with a semi-layered style of mantle convection[49]. This finding has important implications for heat and material cycling across the MTZ, and hence secular planetary cooling. Moreover, substantial quantities of trapped hot materials imply that the MTZ and/or mid-mantle may be on average slightly warmer than predicted by geotherms that are rooted in the upper mantle. A dynamic barrier to flow further leads to imperfect mixing of materials[2,49]. Geochemical constraints indicate that plumes carry compositionally distinct material[3], hence plume stagnation implies that the bulk composition beneath the MTZ differs from that of the upper mantle[4,15,42,50]. Integrating our results with additional geophysical constraints such as from geodynamical modelling and mineral-physics experiments may shed further light on the dynamics of thermochemical plume segregation in the MTZ, in addition to models of mantle evolution.

Online content

Any methods, additional references, Nature Research reporting summaries, source data, extended data, supplementary information, acknowledgements, peer review information; details of author contributions and competing interests; and statements of data and code availability are available at https://doi.org/10.1038/s41561-021-00850-w.

References

1. Burke, K., Steinberger, B., Torsvik, T. & Smethurst, M. Plume generation zones at the margins of large low shear velocity provinces on the core–mantle boundary. *Earth Planet. Sci. Lett.* **265**, 49–60 (2008).
2. Courtillot, V., Davaille, A., Besse, J. & Stock, J. Three distinct types of hotspots in the Earth's mantle. *Earth Planet. Sci. Lett.* **205**, 295–308 (2003).
3. Koppers, A., Staudigel, H., Pringle, M. & Wijbrans, J. Short-lived and discontinuous intraplate volcanism in the South Pacific: hot spots or extensional volcanism? *Geochem. Geophys. Geosys.* https://doi.org/10.1029/2003GC000533 (2003).
4. Nakagawa, T. & Buffett, B. Mass transport mechanism between the upper and lower mantle in numerical simulations of thermochemical mantle convection with multicomponent phase changes. *Earth Planet. Sci. Lett.* **230**, 11–27 (2005).
5. Farnetani, C. & Samuel, H. Beyond the thermal plume paradigm. *Geophys. Res. Lett.* https://doi.org/10.1029/2005GL022360 (2005).
6. Dannberg, J. & Sobolev, S. Low-buoyancy thermochemical plumes resolve controversy of classical mantle plume concept. *Nat. Commun.* **6**, 6960 (2015).
7. Bina, C. & Helffrich, G. Phase transition Clapeyron slopes and transition zone seismic discontinuity topography. *J. Geophys. Res.* **99**, 15853–15860 (1994).
8. Christensen, U. Effects of phase transitions on mantle convection. *Annu. Rev. Earth. Planet. Sci.* **23**, 65–87 (1995).
9. Tackley, P., Stevenson, D., Glatzmaier, G. & Schubert, G. Effects of an endothermic phase transition at 670 km depth in a spherical model of convection in the Earth's mantle. *Nature* **361**, 699–704 (1993).
10. Bercovici, D., Schubert, G. & Tackley, P. On the penetration of the 660 km phase change by mantle downflows. *Geophys. Res. Lett.* **20**, 2599–2602 (1993).
11. Fukao, Y. & Obayashi, M. Subducted slabs stagnant above, penetrating through, and trapped below the 660 km discontinuity. *J. Geophys. Res.* **118**, 5920–5938 (2013).
12. Cao, Q., van der Hilst, R., de Hoop, M. V. & Shim, S. Seismic imaging of transition zone discontinuities suggests hot mantle west of Hawaii. *Science* **332**, 1068–1071 (2011).
13. Ritsema, J., Deuss, A., van Heijst, H. & Woodhouse, J. S40RTS: a degree-40 shear-velocity model for the mantle from new Rayleigh wave dispersion, teleseismic traveltime and normal-mode splitting function measurements. *Geophys. J. Int.* **184**, 1223–1236 (2011).
14. French, S. & Romanowicz, B. Whole-mantle radially anisotropic shear-velocity structure from spectral-element waveform tomography. *Geophys. J. Int.* **199**, 1303–1327 (2014).

15. Ballmer, M. D., Schmerr, N. C., Nakagawa, T. & Ritsema, J. Compositional mantle layering revealed by slab stagnation at ~1000-km depth. *Sci. Adv.* https://doi.org/10.1126/sciadv.1500815 (2015).

16. Tosi, N. & Yuen, D. Bent-shaped plumes and horizontal channel flow beneath the 660 km discontinuity. *Earth Planet. Sci. Lett.* **312**, 348–359 (2011).

17. Jenkins, J., Cottaar, S., White, R. & Deuss, A. Depressed mantle discontinuities beneath Iceland: evidence of a garnet controlled 660 km discontinuity? *Earth Planet. Sci. Lett.* **433**, 159–168 (2016).

18. Hirose, K. Phase transitions in pyrolitic mantle around 670-km depth: implications for upwelling of plumes from the lower mantle. *J. Geophys. Res.* **107**, 2078 (2002).

19. Weidner, D. J. & Wang, Y. Chemical- and Clapeyron-induced buoyancy at the 660 km discontinuity. *J. Geophys. Res. Solid Earth* **103**, 7431–7441 (1998).

20. Shearer, P. & Flanagan, M. Seismic velocity and density jumps across the 410- and 660-kilometer discontinuities. *Science* **285**, 1545–1548 (1999).

21. Houser, C. & Williams, Q. Reconciling Pacific 410 and 660 km discontinuity topography, transition zone shear velocity patterns, and mantle phase transitions. *Earth Planet. Sci. Lett.* **296**, 255–266 (2010).

22. Ritsema, J., Xu, W., Stixrude, L. & Lithgow-Bertelloni, C. Estimates of the transition zone temperature in a mechanically mixed upper mantle. *Earth Planet. Sci. Lett.* **277**, 244–252 (2009).

23. Deuss, A., Redfern, S., Chambers, K. & Woodhouse, J. The nature of the 660-kilometer discontinuity in Earth's mantle from global seismic observations of PP precursors. *Science* **311**, 19–201 (2006).

24. Munch, F., Khan, A., Tauzin, B., van Driel, M. & Giardini, D. Seismological evidence for thermo-chemical heterogeneity in Earth's continental mantle. *Earth Planet. Sci. Lett.* **539**, 116240 (2020).

25. Schmerr, N. & Garnero, E. J. Upper mantle discontinuity topography from thermal and chemical heterogeneity. *Science* **318**, 623–626 (2007).

26. Wu, W., Ni, S. & Irving, J. C. E. Inferring Earth's discontinuous chemical layering from the 660-kilometer boundary topography. *Science* **363**, 763–740 (2019).

27. Waszek, L., Schmerr, N. & Ballmer, M. Global observations of reflectors in the mid-mantle with implications for mantle structure and dynamics. *Nat. Commun.* **9**, 385 (2018).

28. Bassin, C., Laske, G. & Masters, G. The current limits of resolution for surface wave tomography in North America. *EOS Trans. AGU* **81**, F897 (2000).

29. Dziewoński, A. & Anderson, D. Preliminary reference Earth model. *Phys. Earth Planet. Int.* **25**, 297–356 (1981).

30. Lessing, S., Thomas, C., Saki, M., Schmerr, N. & Vanacore, E. On the difficulties of detecting PP precursors. *Geophys. J. Int.* **201**, 1666–1681 (2015).

31. Connolly, J. A. D. Computation of phase equilibria by linear programming: a tool for geodynamic modeling and its application to subduction zone decarbonation. *Earth Planet. Sci. Lett.* **236**, 524–541 (2005).

32. Stixrude, L. & Lithgow-Bertelloni, C. Thermodynamics of mantle minerals – II. Phase equilibria. *Geophys. J. Int.* **184**, 1180–1213 (2011).

33. Baker, M. B. & Stolper, E. M. Determining the composition of high-pressure mantle melts using diamond aggregates. *Geochim. Cosmochim. Acta* **58**, 2811–2827 (1994).

34. Ekström, G., Nettles, M. & Dziewonski, A. The global CMT project 2004-2010: centroid-moment tensors for 13,017 earthquakes. *Phys. Earth Planet. Inter.* **200-201**, 1–9 (2012).

35. Gale, A., Dalton, C. A., Langmuir, C. H., Su, Y. & Schilling, J. The mean composition of ocean ridge basalts. *Geochem. Geophys. Geosys.* https://doi.org/10.1029/2012GC004334 (2013).

36. Afonso, J. C., Fernandez, M., Ranalli, G., Griffin, W. L. & Connolly, J. A. D. Integrated geophysical–petrological modeling of the lithosphere and sublithospheric upper mantle: methodology and applications. *Geochem. Geophys. Geosys.* https://doi.org/10.1029/2007GC001834 (2008).

37. Ringwood, A. E. A model for the upper mantle. *J. Geophy. Res.* **67**, 857–867 (1962).

38. Stixrude, L. & Lithgow-Bertelloni, C. Geophysics of chemical heterogeneity in the mantle. *Annu. Rev. Earth. Planet. Sci.* **40**, 569–595 (2012).

39. Xu, W., Lithgow-Bertelloni, C., Stixrude, L. & Ritsema, J. The effect of bulk composition and temperature on mantle seismic structure. *Earth Planet. Sci. Lett.* **275**, 70–79 (2008).

40. Herzberg, C. et al. Temperatures in ambient mantle and plumes: constraints from basalts, picrites, and komatiites. *Geochem. Geophys. Geosys.* https://doi.org/10.1029/2006GC001390 (2007).

41. Hirose, K., Fei, Y., Ma, Y. & Mao, H. K. The fate of subducted basaltic crust in the Earth's lower mantle. *Nature* **397**, 53–56 (1999).

42. Yan, J., Ballmer, M. D. & Tackley, P. J. The evolution and distribution of recycled oceanic crust in the Earth's mantle: insight from geodynamic models. *Earth Planet. Sci. Lett.* **537**, 116171 (2020).

43. Thio, V., Cobden, L. & Trampert, J. Seismic signature of a hydrous mantle transition zone. *Phys. Earth. Planet. Inter.* **250**, 46–63 (2016).

44. Schulze, K. et al. Seismically invisible water in Earth's transition zone? *Earth Planet. Sci. Lett.* **498**, 9–16 (2018).

45. Müller, R. D., Royer, J. Y. & Lawver, L. A. Revised plate motions relative to the hotspots from combined Atlantic and Indian ocean hotspot tracks. *Geology* **21**, 275–278 (1993).

46. Davaille, A. Simultaneous generation of hotspots and superswells by convection in a heterogeneous planetary mantle. *Nature* **402**, 756–760 (1999).

47. Kim, S. S. & Wessel, P. New global seamount census from altimetry-derived gravity data. *Geophys. J. Int.* **186**, 615–631 (2011).

48. King, S. & Ritsema, J. African hot spot volcanism: small-scale convection in the upper mantle beneath cratons. *Science* **290**, 1137–1140 (2000).

49. Kellogg, L. H. & Turcotte, D. L. Mixing and the distribution of heterogeneities in a chaotically convecting mantle. *J. Geophys. Res. Solid Earth* **95**, 421–432 (1990).

50. Hofmann, A. Mantle geochemistry: the message from oceanic volcanism. *Nature* **385**, 219–229 (1997).

Methods

Adaptive stacking. The PP and SS waveforms require dedicated processing to extract weak reflections from the 410 and 660 (amplitude of 0.4–6% of the reference phase) from the noise. The typical approach is to group the data into bins at the Earth's surface and stack the waveforms. Here, we refine this approach to obtain adaptive stacking (AS), which extracts information about the interface depth and amplitude of reflections with uncertainties. The Earth is partitioned into cells with irregular shapes called Voronoi cells. This parameterization adapts its shape to account for spatial variations in topography. The initial step randomly distributes Voronoi nuclei throughout the globe. The distribution is uniform on the sphere[51], and the initial number of cells (2,000) is chosen such that the surface area covered by an individual cell is smaller than the area of the first Fresnel zone of a single datum. The data are then grouped into the Voronoi cells, according to the location of the reflection points of the reference phase. The grouped time series are converted to depth using PREM[29] after correction for 3D structure, weighted by signal-to-noise ratio, and stacked. The maximum stacked amplitude within a specific depth range surrounding a discontinuity (410 or 660) is defined as the discontinuity depth. The depth windows are 350–480 and 380–440 km for the 410 from SS and PP data, respectively, and 600–730 km (SS) and 610–750 km (PP) for the 660. These ranges were chosen based on synthetic experiments (Fig. 3) and an analysis of the detection performance in the observed datasets. In particular, they account for interference effects from reflections at the 520 km discontinuity, plus the deeper signals from the post-Gt phase dis-association (Fig. 3). Bootstrap resampling provides errors on depth and amplitude estimates[52], which are estimated from one standard deviation of a distribution of 100 samples. In AS, Voronoi cells with post-stacking standard deviations larger than 10 km are removed from the global partition. This procedure iterates until convergence, that is, when all cells have a standard error below 10 km, producing an optimized tessellation for each run. A visual output of the iterative process is presented in Supplementary Fig. 2. A single run produces patterns with sharp edges, and the spatial resolution of the topography variations is influenced by the cell geometry and therefore the initial distribution of the Voronoi cells. Thus, we repeat the process 150 times to obtain measurements across a variety of cell distributions and geometries. We use the outputs of these 150 runs to generate smooth average spatial distributions over a grid of 0.5° × 0.5° in latitude and longitude, producing detailed global maps of discontinuity depths and MTZ thickness (Fig. 2 and Supplementary Figs. 3–5).

Observations of P660P phases and consistency of their timing and slowness. AS cannot be implemented for the P660P because it is weak or absent globally. An absent detection might arise either from the structure of velocity gradients near 660 km depth (Fig. 3a,b,d) or noise in the data. We confirmed with synthetic experiments that topography on the P660P has limited effect at the frequencies of our data (Supplementary Information 5.3). To avoid a null observation due to high noise, we minimize its influence by stacking P660P over the parameterization constructed for the P410P phase. Because this parameterization is optimal for stacking constructively for the 410 km discontinuity topography in terms of data coverage and quality (by suppressing the noise), we expect that it will be similarly successful for the 660 km discontinuity topography. We validated this approach via the SS data, with the result shown in Supplementary Fig. 5. Topographies obtained from stacking the S660S phase based on the S410S and the S660S Voronoi parameterizations are in good agreement (correlation coefficient $R = 0.88$). For P660P detection, we implement a criterion to identify locations with a clear single pulse: Voronoi cells with a standard error for depth of greater than 10 km are defined as 'null' observations. We retain locations at which P660P is detected with at least a 50% probability across the 150 iterative procedures (Fig. 2a and Supplementary Figs. 9, 4d, and 6d).

After global detection of the candidate P660P reflections (Fig. 2a), we performed slant stacking on subsets of the PP data in these regions (Supplementary Fig. 9) for quality evaluation. We show vespagrams for positive and spurious detections in Supplementary Fig. 11. When observed (patches 1–4), the phases have a relative timing of −125 s and a differential slowness of −0.3 s per degree with respect to the PP phase, with no obvious interfering phases. These values are consistent with P wave reflections underneath the 660, as demonstrated by synthetic modelling (Methods).

However, in many cases (patches 5–14), the detections are ambiguous because of the poorly resolved slowness and/or the presence of large-amplitude interfering phases. Systematic analysis of the depth-epicentral distance sections (Supplementary Fig. 12) reveals that the epicentral distance coverage for these patches is quite inhomogeneous, favouring the contribution of interfering phases that mimic P660P (typically PKP, Supplementary Figs. 12–3 and 12 4).

Synthetic modelling from mineral physics (Methods) helps distinguish true P660P detections because the synthetic data incorporate the same acquisition geometry as observed data. We compare observed vespagrams (Supplementary Fig. 11) and depth–distance sections (Supplementary Fig. 12) with predictions using a pyrolitic compositional model, and two reference potential temperatures of 2,000 and 1,400 K. These temperatures were selected as extrema of P660P visibility. A temperature of 1,400 K does not generate a detectable P660P signal, although interfering phases may simulate such an arrival if the epicentral distance

distribution is poor. Conversely, a temperature of 2,000 K consistently generates a large P660P signal. These experiments show that, with good epicentral distance coverage, the data should be able to discriminate between these two temperature regimes. Our criteria for a robust detection (Fig. 2a) are therefore an even, broad distribution of epicentral distance in the time–distance profiles without strong interfering phases, a signal at the relative predicted time and slowness in the observed and 2,000 K synthetic vespagrams, and no signal in the 1,400 K vespagrams. Bootstrap resampling is used to obtain an estimate of the 95% confidence level, to determine whether a signal is significant.

We estimate the average noise level for the 660 depth window via the mean standard deviation on the average trace from bootstrap resampling. The average P660P/PP amplitude ratio is 1.42 ± 0.23%, with an average noise of 0.26 ± 0.11%. At locations with no P660P, we find noise of 0.65 ± 0.21%. A conservative estimate for the minimum detectable P660P amplitude is therefore 0.86%.

Seismic modelling. *Frequency response to complex velocity gradients.* Zoeppritz equations are commonly used to compute reflection/conversion coefficients for first-order seismic interfaces[20,23,53,54]. This approach shows limitations when the discontinuity extends over a wide depth interval. For the MTZ phase transformations, the use of reflection/transmission coefficients for first-order interfaces is valid only at long period[55,56]. To demonstrate the effect of the complex shape of velocity gradients on PP underside reflections (that is, PP precursors), we reconstructed their frequency response by sub-dividing the elastic gradient into thin homogeneous layers, then computing the effective elastic response using a plane-wave matrix algorithm[57–59]. We modified an algorithm from ref. [58] to calculate the generalized reflection–transmission coefficients[56,60].

The result for P-wave reflections underneath various types of structures for the 660 km discontinuity is shown in Supplementary Fig. 16. We show examples of two elastic models for a pyrolitic composition and 1,200 and 2,100 K adiabatic temperature gradients, and of the iasp91 Earth's reference model[61]. The iasp91 structure is a simple first-order discontinuity with approximately 6% v_p and v_s jumps and 7.5% density contrast (Supplementary Fig. 16a). For this structure, the reflection coefficient reaches 4% in the typical 8–40 s period range of analysis, but shows little variation with frequency. Conversely, the responses in frequency of mineral-physics-based models display substantial deviation from those of a first-order interface. At long periods, the elastic gradients appear as a first-order discontinuity to seismic waves. The reflection coefficient is maximum for the 2,100 K elastic profile because the overall contrast in elastic properties is larger for this model. The 1,200 K model is the least efficient for reflecting long-period P-waves.

For the two mineralogical models, the shape of the response (a low-pass filter) is typical of that from an extended elastic gradient: the larger the gradient, the lower the cut-off filter frequency (Supplementary Fig. 16b). For SS precursors and other phases, the response of these structures is instead flat within the band pass of analysis of the data (not shown here). Particularly noteworthy is that the roll-off of the filter for these structures for PP precursors occurs at the lower limit of the typical frequency range for analysis of PP precursors. Thus, the reflective characteristics of the 660 for PP-like waves have complex fluctuations depending on the frequency content of the data and the wave slowness. In the frequency range of analysis, and for the same jump in elastic properties, the reflections have lower amplitudes for gradual boundaries than for a single first-order interface. The 2,100 K model is more reflective than the 1,200 K model (1% for the 1,200 K model and 2% for the 2,100 K model, versus 4% for iasp91).

A database of full-waveform synthetic seismograms. Accurate seismic modelling is crucial to test the effects of the processing on time-domain signals, and the influence of stacking seismic data with different source mechanisms and source–receiver geometry. The acquisition geometry controls in particular interference patterns from other seismic phases. In addition, seismic modelling allows us to quantitatively investigate the effect of temperature on the waveforms. We use a reflectivity algorithm[62,63] to model the complete waveform on synthetic vertical and transverse components for each seismogram in our databases, performed in one-dimensional (1D) Earth's seismic models.

Instead of simulating wave propagation for 2,036 PP and 1,666 SS sources, we generate a library of seismograms for five elementary moment tensors (Supplementary Fig. 14) taken as sources located at depths from 2.5 to 75 km in steps of 2.5 km. Seismograms are reconstructed from a linear combination of these elementary seismograms[64]. An example of a reconstruction and comparison with observed data is presented in Supplementary Fig. 14. We confirmed for arbitrary moment tensors that the reconstructions provide the same waveforms as when computing the seismograms using these moment tensors (Supplementary Fig. 14). In each simulation, 200 receivers are located at distances from 80° to 179.5°, every 0.5°. This reduces the number of simulations to 150 per seismic model. In the library of elementary seismograms, the sampling precisions in the event depths and epicentral distances introduce an error in the reconstruction. However, the effect is small as the measurements are ultimately performed for stacked seismograms. We add random noise to the synthetics (Supplementary Fig. 15), from a uniform distribution within 1–30% of the amplitude of the reference phase. This procedure reproduces the noise effect in the observed data. The noise is filtered for the

same frequencies before application. The synthetic databases are then processed in a similar way to the observed data (AS, with the same procedure for retaining locations with P660P signals) for comparison.

Elastic models from mineral physics. The reference compositional model in our study is pyrolite, which is a model composition for the Earth's upper mantle[37]. Its phase transformations are in qualitative agreement with observed seismic discontinuities (Fig. 3a). The composition is based on the analysis from ref. [33] with weight percentages of oxides of 45.5% for SiO_2, 3.98% for Al_2O_3, 7.18% for FeO, 38.3% for MgO and 3.57% for CaO. Qualitative comparison with other studies using slightly different pyrolitic compositions does not show obvious difference in the phase diagram[22,32,39]. Phase assemblages are obtained via Gibbs free energy minimization with the Perple_X code[31], using the thermodynamic formalism and mineral elastic properties database (v_p, v_s and density) from ref. [32]. This computation supposes that the chemistry of the mantle is fully equilibrated (EA). We test other models based on mechanical mixtures (MM) of harzburgite and basalt (the properties of these two lithologies also being computed in the same manner). A mixture of these two harzburgite–basalt compositions is supposed to represent at first order mantle material that has undergone complete differentiation at mid-oceanic ridges and is cycled back into the mantle at subduction zones. We test various mechanical mixtures parameterized in terms of fraction of basalt. The overall physical properties of the assemblages are shown in Supplementary Fig. 17, computed from a weighted average of the constituents (Voigt average). We find differences in elastic properties computed with Reuss, Voigt and Voigt–Reuss–Hill averages to be insignificant.

Properties are computed along pressure–temperature adiabatic gradients, with corresponding potential temperatures associated with the extrapolation of the adiabat to the Earth's surface. The pressure step size is sampled such that the elastic profiles are discretized with approximately 4 km depth interval. This allows us to accurately model frequency-dependent waveforms within the frequency range of analysis. We compute 1D elastic profiles for 19 adiabats with potential temperatures ranging from 600 K to 2,400 K in steps of 100 K (Fig. 3b and Supplementary Fig. 17). The shear and compressional seismic attenuations are fixed to the attenuation profiles in PREM[20]. A difference in the viscoelastic behaviour should be expected from accounting for grain boundary sliding through extended Burgers' models[65], but synthetic experiments (see, for example, ref. [66]) showed that this effect is small relative to PREM attenuation. The overall effect of increased attenuation is mainly seen for shear waves (that is, SS) at high temperatures, with less impact on PP waveforms. We simulate teleseismic wave propagation in each of these 19 models, building the libraries of seismograms as described above to generate synthetic data corresponding to every seismogram in the observed databases.

Theoretical PP and SS waveforms for the reference pyrolitic composition (EA) and various mixtures of basalt and harzburgite (MM) are shown in Fig. 3c,d and Supplementary Figs. S18 and S19, respectively. The trends in the thermal response of the P660P reflection are consistent across the compositional models, with low reflection amplitudes at intermediate/high temperatures (below 1,700–1,800 K), and higher amplitudes above this temperature threshold (Supplementary Fig. 19). In comparison, SS data do not show obvious temperature-dependent variations in reflection amplitudes (Supplementary Figs. 18 and 22). Increasing the basalt fraction decreases the overall impedance contrast across the phase changes between Ol polymorphs but increases the impedance contrast across transitions in the Gt system (Supplementary Fig. 17). This behaviour is mapped into the amplitudes of pulses of PP and SS waves reflected at the velocity gradients (Supplementary Figs. 18 and 19).

Uncertainties in predicted MTZ thickness and depth gradients for seismic velocities derived from thermodynamic calculations have been discussed in a number of works (see, for example, refs. [41,67–70], and references therein). These studies concluded that the main sources of intrinsic error (that is, those not related to uncertainties in T and p) come from uncertainties in bulk composition, stability of mineral phases and elastic properties of some end-member minerals, especially the Gt and pyroxene end-members, the latter two being generally more important. According to previous results[69,70], we estimate uncertainties (one standard deviation) of the order of ±5 km for the MTZ thickness and approximately 10% for the depth gradients (dv_p/dp).

Predictions for amplitudes of P410P, S410S and S660S are shown in Supplementary Fig. 20 and for P660P amplitudes in Fig. 3f, in comparison with global observations. The observed S410S, S660S and P660P amplitude distributions all fall within the range predicted by basalt fractions of 0–0.6. Observed P410P amplitudes are slightly larger than predicted. This discrepancy between observations and theory may arise from variations in chemistry, uncertainties in the thermoelastic mineral properties and inaccuracies in tomographic corrections or the seismic forward modelling.

Joint inversion for temperature and composition. To determine the temperature and composition that best match our combination of SS and PP measurements, we perform statistical inversions of the MTZ thickness, and amplitudes of S410S, S660S, P410P and P660P, exploring the entire model space of (T_{pot}, f). These data have very different sensitivity to T_{pot} and f. Supplementary Fig. 22 shows

that the S410S, S660S and P410P amplitudes depend almost entirely on mantle composition, whereas for basalt fractions of 0–0.6, the MTZ thickness is controlled by temperature. P660P amplitudes have a more complicated dependence on both T_{pot} and f. Supplementary Fig. 22 shows the range of properties that satisfies each data individually, for regions away from clear P660P observations (that is, 95% of the Earth's surface).

These seismic observables are then used to perform a probabilistic inversion for (T_{pot}, f) (Supplementary Figs. 23 and 24). For this, we consider (1) locations away from a clear P660P signal (amplitudes below the noise level of 0.65−0.21 = 0.44%), and (2) regions with clear P660P observations. We use a Bayesian formulation, the posterior distribution on model parameters m given the data d being such that

$$\mathrm{P}\,(m|d) \propto \mathrm{P}\,(d|m)\,\mathrm{P}\,(m)\,,$$

where $\mathrm{P}(m)$ is the prior distribution on model parameters (T_{pot}, f), and $\mathrm{P}(d|m)$ is the likelihood of observing the data d (SS, PP precursor amplitudes or the MTZ thickness) from (T_{pot}, f). We use uniform priors within [0; 1] and [1,000; 2,400] K for f and T_{pot}. The likelihood represents the misfit between observed d^{obs} and predicted data d:

$$\mathrm{P}\,(d|m) = \exp\left(-1/2\left(d^{obs} - d\right)^2/\sigma^2\right),$$

d^{obs} being either the average MTZ thickness or SS/PP precursor amplitudes over the considered regions, and σ representing one standard deviation on spatial variations over the region. Supplementary Figs. 23 and 24 show individual likelihoods for each data taken separately, with the highest probability centred on the range of properties that satisfies the data (Supplementary Fig. 22). The joint posterior probability distribution (Supplementary Fig. 23b and 24b) is then computed as $\mathrm{P}(m|d) = \prod_i p_i(m|d_i)$, where i is the index of the dataset (amplitude or thickness). These posterior distributions are approximately two-dimensional Gaussian functions with a well-defined (T_{pot}, f) maximum and a small positive trade-off. Best-fit solutions and standard deviations on T_{pot} and f are measured from the marginal posterior distributions (Supplementary Fig. 23b and 24b).

Data availability
Waveform data are publicly available from the IRIS Data Management Center (NSF grant EAR-1063471). Measurements of the 410 and 660 km discontinuities, the thermal map and velocity models are available from the ISC Repository (https://doi.org/10.31905/7M3LMG8X).

Code availability
A downsampled database of synthetic seismograms for mineral-physics models is available from https://zenodo.org/record/5512035. A simplified version of the adaptive stacking code is available from https://zenodo.org/record/5512805. The full database and software are available from the corresponding author upon request.

References
51. Marsaglia, G. Choosing a point from the surface of a sphere. *Ann. Math. Stat.* **43**, 645–646 (1972).
52. Efron, B. & Tibshirani, R. *An Introduction to the Bootstrap* (Chapman and Hall, 1991).
53. Zoeppritz, K. On the reflection and penetration of seismic waves through unstable layers. *Gött. Nachr.* **1**, 66–84 (1919).
54. Aki, K. & Richards., P. G. *Quantitative Seismology: Theory and Methods*, p. 801 (W. H. Freeman, 1980).
55. Bostock, M. G. Seismic waves converted from velocity gradient anomalies in the Earth's upper mantle. *Geophys. J. Int.* **138**, 747–756 (1999).
56. Tauzin, B., Pham, T. S. & Tkalčić, H. Receiver functions from seismic interferometry: a practical guide. *Geophys. J. Int.* **217**, 1–24 (2019).
57. Kennett, B. N. L. *Seismic Wave Propagation in Stratified Media*, p. 288 (ANU Press, 1983).
58. Chapman, C. H. Yet another elastic plane-wave, layer-matrix algorithm. *Geophys. J. Int.* **154**, 212–223 (2003).
59. Chapman, C. H. *Fundamentals of Seismic Wave Propagation* (Cambridge Univ. Press, 2004).
60. Ma, Y., Wang, R. & Zhou, H. A note on the equivalence of three major propagator algorithms for computational stability and efficiency. *Earthq. Sci.* **25**, 55–64 (2012).
61. Kennett, B. N. L. & Engdahl, E. Traveltimes for global earthquake location and phase identification. *Geophys. J. Int.* **105**, 429–465 (1991).
62. Fuchs, K. & Müller, G. Computation of synthetic seismograms with the reflectivity method and comparison with observations. *Geophys. J. Int.* **23**, 417–433 (1971).
63. Müller, G. The reflectivity method: a tutorial. *J. Geophysics* **58**, 153–174 (1985).
64. Kikuchi, M. & Kanamori, H. Inversion of complex body waves—III. *Bull. Seism. Soc. Am.* **81**, 2335–2350 (1991).

65. Faul, U. H. & Jackson, I. The seismological signature of temperature and grain size variations in the upper mantle. *Earth Planet. Sci. Lett.* **234**, 119–134 (2005).

66. Munch, F. D., Khan, A., Tauzin, B., Zunino, A. & Giardini, D. Stochastic inversion of P-to-S converted waves for mantle composition and thermal structure: methodology and application. *J. Geophys. Res. Solid Earth* **123**, 10–706 (2018).

67. Connolly, J. A. D. & Kerrick, D. M. Metamorphic controls on seismic velocity of subducted oceanic crust at 100–250 km depth. *Earth Planet. Sci. Lett.* **204**, 61–74 (2002).

68. Afonso, J. C. et al. 3-D multiobservable probabilistic inversion for the compositional and thermal structure of the lithosphere and upper mantle I: a priori information and geophysical observables. *J. Geophys. Res. Solid Earth* **118**, 2586–2617 (2013).

69. Stixrude, L. & Jeanloz, R. *Constraints on Seismic Models from Other Disciplines - Constraints from Mineral Physics on Seismological Models* (Elsevier, 2015).

70. Connolly, J. A. D. & Khan, A. Uncertainty of mantle geophysical properties computed from phase equilibrium models. *Geophys. Res. Lett.* **43**, 5026–5034 (2016).

Author contributions

The study was conceived by L.W. and B.T. The datasets were compiled by L.W., partially supervised by N.C.S. B.T. wrote the adaptive stacking and synthetic modelling codes, with some contribution by L.W. B.T. and L.W. ran the synthetic experiments. L.W. implemented the analysis on observed data. All authors discussed the results and interpretations, and contributed to the manuscript.

Competing interests

The authors declare no competing interests.

Additional information

Supplementary information The online version contains supplementary material available at https://doi.org/10.1038/s41561-021-00850-w.

Correspondence and requests for materials should be addressed to Lauren Waszek.

Peer review information *Nature Geoscience* thanks Sidao Ni, Saskia Goes and Johannes Buchen for their contribution to the peer review of this work. Primary Handling editors: Stefan Lachowycz and Simon Harold.

Reprints and permissions information is available at www.nature.com/reprints.